Structural Engineering and Mechanics, *Vol. 73, No. 1 (2020) 1-16*
DOI: https://doi.org/10.12989/sem.2020.73.1.001

New higher-order triangular shell finite elements based on the partition of unity

Hyungmin Jun*[1,2]

[1]*Department of Mechanical System Engineering, Jeonbuk National University, 567 Baekje-daero, Deokjin-gu, Jeonju-si, Jeollabuk-do 54896, Republic of Korea*
[2]*Department of Biological Engineering, Massachusetts Institute of Technology, 77 Massachusetts Avenue, Cambridge, MA 02139, USA*

(Received July 3, 2019, Revised July 10, 2019, Accepted October 4, 2019)

Abstract. Finite elements based on the partition of unity (PU) approximation have powerful capabilities for p-adaptivity and solutions with high smoothness without remeshing of the domain. Recently, the PU approximation was successfully applied to the three-node shell finite element, properly eliminating transverse shear locking and showing excellent convergence properties and solution accuracy. However, the enrichment with the PU approximation results in a significant increase in the number of degrees of freedom; therefore, it requires greater computational cost, thus making it less suitable for practical engineering. To circumvent this disadvantage, we propose a new strategy to decrease the total number of degrees of freedom in the existing PU-based shell element, without loss of optimal convergence and accuracy. To alleviate the locking phenomenon, we use the method of mixed interpolation of tensorial components and perform convergence studies to show the accuracy and capability of the proposed shell element. The excellent performances of the new shell elements are illustrated in three benchmark problems.

Keywords: partition of unity; shell finite element; three-node element; MITC method; convergence study; benchmark test

1. Introduction

For several decades, many research efforts have been devoted to developing an efficient and accurate finite element and have made astounding successes in many areas of structural engineering and sciences. Nevertheless, the performance of the displacement-based linear element is not satisfactory because it cannot properly represent pure bending displacement fields. Thus, in pure bending, the linear finite element exhibits spurious shear energy (Hughes 2012, Cook 2007, Bathe 2016), also called “parasitic” energy since it should not appear in bending situations. In an effort to improve the linear finite element, a promising approach called the partition of unity method (PUM) (Melenk and Babuška 1996, Babuška and Melenk 1997) has been proposed in recent years and successfully applied in many fields. This approach is based on the partition of unity (PU) approximation and developed into different types of PU methods, such as the numerical manifold method (Shi 1991, Zheng and Xu 2014), *hp*-clouds (Oden *et al.* 1998), the PU-based finite element method (Tian *et al.* 2006, Rajendran and Zhang 2007, Zhang and Rajendran 2008, Cai *et al.* 2010, Xu and Rajendran 2013, Yang *et al.* 2017), the generalized finite element method (GFEM) (Duarte *et al.* 2000, Strouboulis *et al.* 2000, Duarte *et al.* 2001, Strouboulis *et al.* 2001), and the extended finite element method (XFEM) (Moës and Belytschko 2002, Belytschko *et al.* 2009, Shojaee *et al.* 2013). The PU-based methods feature mainly that the high-order global approximation of any degree can be constructed without adding extra nodes. The PU-based methods provide good accuracy for both displacement and stresses in pure bending, and they present low sensitivity to element distortion.

Recently, shell finite elements were successfully enriched with the PU approximation to obtain quadratic displacement interpolations without any mesh refinement (Jeon *et al.* 2014, Jun *et al.* 2018a), alleviating the transverse shear locking effect using the Mixed Interpolation of Tensorial Components (MITC) method (Bathe and Dvorkin 1986, Lee and Bathe 2004, Lee *et al.* 2008, Jeon *et al.* 2014, Lee *et al.* 2015, Jeon *et al.* 2015, Jun *et al.* 2018a, Katili *et al.* 2019). The high numerical performance of the enrichment scheme with the PU approximation was validated, showing optimal convergence and accuracy in several shell problems. The effectiveness of using the enrichment scheme only locally was also illustrated in critical areas of an analysis shell domain. Despite substantial advancements in the solution accuracy and efficient use in critical areas of an analysis domain, it remains challenging to decrease the total degrees of freedom (DOFs) for the PU-based shell element with 15 DOFs, including nine DOFs for displacements and six DOFs for rotations per node.

The aim of this study is to present an efficient PU-based shell finite element, without loss of solution accuracy, that is comparable to a higher-order six-node shell element. Here, new PU-based triangular shell elements are introduced by applying the PU approximation with both membrane displacements and rotations and only with rotations of the shell. The former shell element has 13

*Corresponding author, Ph.D.
E-mail: hjun@jbnu.ac.kr

http://www.techno-press.com/journals/sem&subpage=7
ISSN: 1225-4568 (Print), 1598-6217 (Online)

DOFs, including seven DOFs for displacements and six DOFs for rotations, whereas the latter shell element includes nine DOFs, including three DOFs for displacements and six DOFs for rotations. The MITC method is adopted to eliminate transverse shear locking, treating the assumed covariant transverse share strain fields separately for the standard linear and the additional quadratic displacement interpolations in the same way as in the previously published PU-based shell element (Jeon *et al.* 2014). Two proposed shell finite elements also pass three basic tests: the isotropy, the patch, and the zero-energy mode test.

In the following sections, the formulations of the new PU-based shell finite elements are presented. The convergence studies are conducted with a fully clamped square plate problem, cylindrical shell problems, and hyperboloid shell problems, comparing the standard three- and six-node shell elements as well as the previously developed PU-based shell element. Then, the key numerical aspects of our scheme regarding the computational expenses are discussed. For a further examination, three illustrative benchmark tests, a hyperboloid paraboloid shell problem, a hemisphere shell problem, and a roof shell problem, are computed to evaluate the performance of the proposed shell elements using three different mesh patterns, including distorted meshes.

2. The formulations of the new PU-based shell finite elements

The displacement interpolations of the proposed shell finite elements based on the PU approximation are introduced in this section. The present shell finite elements use the MITC technique to construct appropriate assumed strain interpolations.

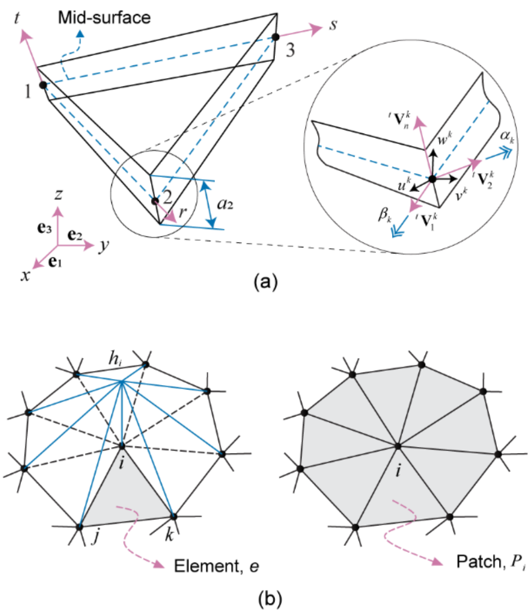

Fig. 1 The geometry of the three-node shell element and the description of the subdomain: (a) Geometry and definition of the rotational degrees of freedom α_k and β_k. (b) The patch P_i constructed by all the elements connected to node i

2.1 Standard three-node shell finite element

The geometry of the continuum mechanics based three-node triangular shell finite element, as shown in Fig. 1(a), is given by (Lee and Bathe 2004, Bathe 2016, Jeon *et al.* 2014)

$$\bar{\mathbf{x}}(r,s,t) = \sum_{i=1}^{3} h_i(r,s)\bar{\mathbf{x}}_i + \frac{t}{2}\sum_{i=1}^{3} a_i h_i(r,s)\mathbf{V}_n^i \quad \text{with } h_1 = r,\ h_2 = s,\ h_3 = 1-r-s, \tag{1}$$

where r, s, and t are natural coordinates, $h_i(r,s)$ is the 2D interpolation function corresponding to node i, $\bar{\mathbf{x}}_i$ is the position vector of node i in the global Cartesian coordinate system, and a_i and $\mathbf{V}_n^i$ denote the shell thickness and the director vector at node i, respectively.

The displacement interpolation of the three-node shell element is given by

$$\bar{\mathbf{u}}(r,s,t) = \sum_{i=1}^{3} h_i(r,s)\bar{\mathbf{u}}_i + \sum_{i=1}^{3}\frac{t}{2} a_i h_i(r,s)\left(-\mathbf{V}_2^i\bar{\alpha}_i + \mathbf{V}_1^i\bar{\beta}_i\right), \tag{2}$$

in which $\bar{\mathbf{u}}_i = [\bar{u}_i \ \ \bar{v}_i \ \ \bar{w}_i]^{\mathrm{T}}$ is the nodal displacement vector in the global Cartesian coordinate system, $\mathbf{V}_1^i = [V_{1x}^i \ \ V_{1y}^i \ \ V_{1z}^i]^{\mathrm{T}}$ and $\mathbf{V}_2^i = [V_{2x}^i \ \ V_{2y}^i \ \ V_{2z}^i]^{\mathrm{T}}$ are unit vectors orthogonal to $\mathbf{V}_n^i$ and to each other, and $\bar{\alpha}_i$ and $\bar{\beta}_i$ are the rotations of the director vector $\mathbf{V}_n^i$ about $\mathbf{V}_1^i$ and $\mathbf{V}_2^i$ at node i.

2.2 Partition of unity approximation

The enrichment of the three-node triangular shell element with the PU approximation proceeds as described previously (Jeon *et al.* 2014, Jun *et al.* 2018a). The patch P_i is composed of elements surrounding node i, as shown in Fig. 1(b), and the local approximation functions are defined on the patch. The partition of unity subordinate to each patch is a set of functions such that for every point in the domain under consideration it sums to one. Since the finite element shape function forms a partition of unity, local approximations are defined by linear piecewise polynomials. Thus, the displacement interpolations for the PU-based shell element are obtained as

$$\begin{aligned}\mathbf{u}(r,s,t) &= \sum_{i=1}^{3} h_i(r,s)\mathbf{u}_i^l(\mathbf{x}) \\ &+ \frac{t}{2}\sum_{i=1}^{3} a_i h_i(r,s)\left(-\mathbf{V}_2^i\alpha_i^l(\mathbf{x}) + \mathbf{V}_1^i\beta_i^l(\mathbf{x})\right)\end{aligned}, \tag{3}$$

where $\mathbf{u}_i^l(\mathbf{x})$ is the local approximation function for the displacement, and $\alpha_i^l(\mathbf{x})$ and $\beta_i^l(\mathbf{x})$ are the local functions for the director vectors.

Unlike in the previously published PU-based shell element (Jeon *et al.* 2014), the local approximations constructed with linear polynomials are applied only to membrane displacements and rotations of the shell element.

With the enrichment of membrane displacements and rotations, the shell element can properly represent the pure bending due to additional higher-order displacement and rotation fields.

It is noteworthy that the linear polynomials x and y in the local functions are projected to the membrane surface of the shell by the director vectors, which is not considered in the PU-based shell element published previously (Jeon *et al.* 2014). The local functions are defined as follows:

$$\begin{aligned}\mathbf{u}_i^l(\mathbf{x}) = \left[a_{0i}^u + \left(\mathbf{x}\cdot\mathbf{V}_1^i\right)a_{1i}^u + \left(\mathbf{x}\cdot\mathbf{V}_2^i\right)a_{2i}^u\right]\mathbf{V}_1^i \\ + \left[a_{0i}^v + \left(\mathbf{x}\cdot\mathbf{V}_1^i\right)a_{1i}^v + \left(\mathbf{x}\cdot\mathbf{V}_2^i\right)a_{2i}^v\right]\mathbf{V}_2^i\end{aligned}, \tag{4}$$

$$\alpha_i^l(\mathbf{x}) = \left[a_{0i}^\alpha + \left(\mathbf{x}\cdot\mathbf{V}_1^i\right)a_{1i}^\alpha + \left(\mathbf{x}\cdot\mathbf{V}_2^i\right)a_{2i}^\alpha\right], \text{ and} \tag{5}$$

$$\beta_i^l(\mathbf{x}) = \left[a_{0i}^\beta + \left(\mathbf{x}\cdot\mathbf{V}_1^i\right)a_{1i}^\beta + \left(\mathbf{x}\cdot\mathbf{V}_2^i\right)a_{2i}^\beta\right], \tag{6}$$

in which a_{0i}^u to a_{2i}^u, a_{0i}^v to a_{2i}^v, a_{0i}^α to a_{2i}^α, and a_{0i}^β to a_{2i}^β are the corresponding unknown coefficients to be determined. The local approximation functions can be rewritten by enforcing $\mathbf{u}_i^l(\mathbf{x})$, $\alpha_i^l(\mathbf{x})$, and $\beta_i^l(\mathbf{x})$ to be equal to the nodal value at node i and subtracting them from Eqs. (4)-(6):

$$\mathbf{u}_i^l(\mathbf{x}) = \bar{\mathbf{u}}_i + \left(\xi_i\hat{u}_i^\xi + \eta_i\hat{u}_i^\eta\right)\mathbf{V}_1^i + \left(\xi_i\hat{v}_i^\xi + \eta_i\hat{v}_i^\eta\right)\mathbf{V}_2^i, \tag{7}$$

$$\alpha_i^l(\mathbf{x}) = \bar{\alpha}_i + \xi_i\hat{\alpha}_i^\xi\mathbf{V}_1^i + \eta_i\hat{\alpha}_i^\eta\mathbf{V}_2^i, \text{ and} \tag{8}$$

$$\beta_i^l(\mathbf{x}) = \bar{\beta}_i + \xi_i\hat{\beta}_i^\xi\mathbf{V}_1^i + \eta_i\hat{\beta}_i^\eta\mathbf{V}_2^i, \tag{9}$$

with $\xi_i = \left(\mathbf{x}-\bar{\mathbf{x}}_i\right)\cdot\mathbf{V}_1^i$, $\eta_i = \left(\mathbf{x}-\bar{\mathbf{x}}_i\right)\cdot\mathbf{V}_2^i$, $\hat{u}_i^\xi = a_{1i}^u$, $\hat{u}_i^\eta = a_{2i}^u$, $\hat{v}_i^\xi = a_{1i}^v$, $\hat{v}_i^\eta = a_{2i}^u$, $\hat{\alpha}_i^\xi = a_{1i}^\alpha$, $\hat{\alpha}_i^\eta = a_{2i}^\alpha$, $\hat{\beta}_i^\xi = a_{1i}^\beta$, and $\hat{\beta}_i^\eta = a_{2i}^\beta$.

In Eqs. (7)-(9), to improve the conditioning of the stiffness matrix, it is effective to scale the values ξ_i and η_i by the diameter of the largest finite element sharing the node i, $\tilde{h}_i$ (Tian *et al.* 2006, Jeon *et al.* 2014, Jun *et al.* 2018a):

$$\xi_i = \left(\mathbf{x}-\bar{\mathbf{x}}_i\right)\cdot\mathbf{V}_1^i / \tilde{h}_i \text{ and } \eta_i = \left(\mathbf{x}-\bar{\mathbf{x}}_i\right)\cdot\mathbf{V}_2^i / \tilde{h}_i. \tag{10}$$

Substituting Eqs. (7)-(10) into Eq. (3) yields the displacement interpolation for the new PU-based shell element (hereafter denoted as S3PU8), which has eight additional DOFs compared to the standard three-node shell element:

$$\mathbf{u}_{\text{S3PU8}}(r,s,t) = \bar{\mathbf{u}}(r,s,t) + \hat{\mathbf{u}}_{\text{mem}}(r,s) + \hat{\mathbf{u}}_{\text{rot}}(r,s,t) \tag{11}$$

with

$$\begin{aligned}&\hat{\mathbf{u}}_{\text{mem}}(r,s) \\ &= \sum_{i=1}^{3} h_i\left[(\xi_i\hat{u}_i^\xi + \eta_i\hat{u}_i^\eta)\mathbf{V}_1^i + (\xi_i\hat{v}_i^\xi + \eta_i\hat{v}_i^\eta)\mathbf{V}_2^i\right] \text{ and}\end{aligned} \tag{12}$$

$$\begin{aligned}&\mathbf{u}_{\text{rot}}(r,s,t) = \frac{t}{2}\sum_{i=1}^{3} a_i h_i(r,st)\left(\Theta + \Phi\right) \text{ with} \\ &\Theta = (-\mathbf{V}_2^i\hat{\alpha}_i^\xi + \mathbf{V}_1^i\hat{\beta}_i^\xi)\xi\mathbf{V}_1^i \text{ and} \\ &\Phi = (-\mathbf{V}_2^i\hat{\alpha}_i^\eta + \mathbf{V}_1^i\hat{\beta}_i^\eta)\eta_i\mathbf{V}_2^i.\end{aligned} \tag{13}$$

By applying the PU approximation with the rotations of the shell, we obtain the new shell element (hereafter denoted as S3PU4) with four additional DOFs. The displacement interpolation for the S3PU4 shell element is obtained by

$$\mathbf{u}_{\text{S3PU4}}(r,s,t) = \bar{\mathbf{u}}(r,s,t) + \hat{\mathbf{u}}_{\text{rot}}(r,s,t). \tag{14}$$

The previously developed PU-based shell element (Jeon *et al.* 2014) (hereafter denoted as enriched MITC3 and En MITC3 in the legends of the figures) contains the enriched displacement fields for the displacements w, as follows:

$$\mathbf{u}_{\text{Enriched MITC3}}(r,s,t) = \bar{\mathbf{u}}(r,s,t) + \hat{\mathbf{u}}_{\text{disp}}(r,s) + \hat{\mathbf{u}}_{\text{rot}}(r,s,t) \tag{15}$$

with

$$\begin{aligned}&\hat{\mathbf{u}}_{\text{disp}}(r,s) = \sum_{i=1}^{3} h_i(r,s)\Psi \text{ with} \\ &\Psi = (\xi_i\hat{u}_i^\xi + \eta_i\hat{u}_i^\eta) + (\xi_i\hat{v}_i^\xi + \eta_i\hat{v}_i^\eta) + (\xi_i\hat{w}_i^\xi + \eta_i\hat{w}_i^\eta),\end{aligned} \tag{16}$$

in which $\hat{w}_i^\xi$ and $\hat{w}_i^\eta$ are the additional unknown coefficients corresponding to the enriched displacement field for the displacement w.

In the use of the above mentioned displacement interpolations, the linear dependence problem is suppressed by simply enforcing zero displacements on the boundary, not only $\bar{\mathbf{u}}_i = 0$ but also $\hat{u}_i^\xi = \hat{u}_i^\eta = v_i^\xi = \hat{v}_i^\eta = \hat{w}_i^\xi = \hat{w}_i^\eta = \hat{\alpha}_i^\xi = \hat{\alpha}_i^\eta = \hat{\beta}_i^\xi = \hat{\beta}_i^\eta = 0$; see References (Tian *et al.* 2006, Jeon *et al.* 2014, Jun *et al.* 2018a).

2.3 Assumed covariant transverse shear strain fields

The linear part of the Green-Lagrange strain tensor is used, and its covariant strain components are directly obtained by

$$e_{ij} = \frac{1}{2}\left(\mathbf{u}_{,i}\cdot\bar{\mathbf{g}}_j + \bar{\mathbf{g}}_i\cdot\mathbf{u}_{,j}\right), \tag{17}$$

$$\begin{aligned}&\text{where } \bar{\mathbf{g}}_i = \frac{\partial\bar{\mathbf{x}}}{\partial r_i}, \; \mathbf{u}_{,i} = \frac{\partial\mathbf{u}}{\partial r_i} = \frac{\partial\left(\bar{\mathbf{u}}+\hat{\mathbf{u}}\right)}{\partial r_i} = \bar{\mathbf{u}}_{,i} + \hat{\mathbf{u}}_{,i} \\ &\text{with } r_1 = r, \; r_2 = s \text{ and } r_3 = t.\end{aligned} \tag{18}$$

Then, the covariant strain components are separated into linear and additional quadratic terms, as follows:

$$e_{ij} = \bar{e}_{ij} + \hat{e}_{ij} \tag{19}$$

with

$$\bar{e}_{ij} = \frac{1}{2}\left(\bar{\mathbf{u}}_{,i}\cdot\bar{\mathbf{g}}_j + \bar{\mathbf{g}}_i\cdot\bar{\mathbf{u}}_{,j}\right) \text{ and} \tag{20}$$

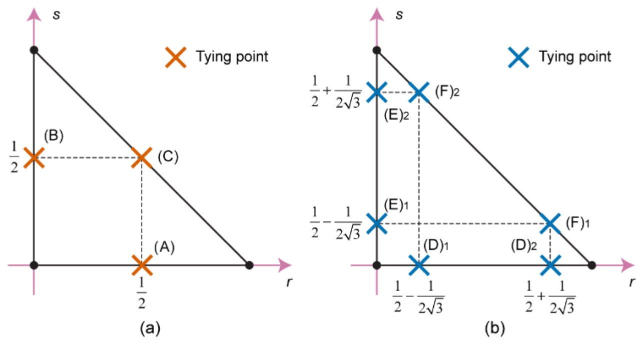

Fig. 2 Tying points for the assumed transverse shear strains of the proposed shell finite elements: for the standard linear (a) and additional quadratic (b) interpolations for the displacement interpolation

$$\hat{e}_{ij} = \frac{1}{2}\left(\hat{\mathbf{u}}_{,i} \cdot \bar{\mathbf{g}}_j + \bar{\mathbf{g}}_i \cdot \hat{\mathbf{u}}_{,j}\right). \quad (21)$$

To reduce the transverse shear locking, we use the MITC method for the covariant transverse shear strains. Two different assumed transverse shear strain fields for the standard three- and six-node shell elements (Lee and Bathe 2004) are employed for the standard and additional quadratic strains $\bar{e}_{ij}$ and $\hat{e}_{ij}$, respectively, in exactly the same manner as for the enriched MITC3 shell element (Jeon *et al.* 2014). The treatment for the membrane locking is not necessary and not used for the proposed shell element because of its flat geometry.

The assumed strain field used for the standard displacement interpolation is

$$\bar{e}_{rt}^{AS} = \bar{e}_{rt}^{(A)} + cs \quad \text{and} \quad \bar{e}_{st}^{AS} = \bar{e}_{st}^{(B)} - cr\,, \quad (22)$$

where $c = \bar{e}_{st}^{(B)} - \bar{e}_{rt}^{(A)} - \bar{e}_{st}^{(C)} + \bar{e}_{rt}^{(C)}$ and, at the tying points, $\bar{e}_{rt}^{(N)}$ and $\bar{e}_{st}^{(N)}$ are calculated from Eq. (20). The tying points (A3), (B3), and (C3) are presented in Fig. 2(a).

The assumed covariant transverse shear strain field for the additional quadratic displacement interpolation is

$$\hat{e}_{rt}^{AS} = a_1 + b_1 r + c_1 s\,, \quad (23)$$

$$\hat{e}_{st}^{AS} = a_2 + b_2 r + c_2 s\,, \quad (24)$$

and the coefficients are given by

$$a_1 = m_{rt}^{(D)} - l_{rt}^{(D)}, \quad b_1 = 2l_{rt}^{(D)}, \quad (25)$$

$$a_2 = m_{st}^{(E)} - l_{st}^{(E)}, \quad c_2 = 2l_{st}^{(E)}, \quad (26)$$

$$c_1 = (a_2 + c_2 - a_1) - (m_{st}^{(F)} + l_{st}^{(F)} - m_{rt}^{(F)} - l_{rt}^{(F)}), \quad (27)$$

$$b_2 = (a_1 + b_1 - a_2) + (m_{st}^{(F)} - l_{st}^{(F)} - m_{rt}^{(F)} + l_{rt}^{(F)}) \quad (28)$$

$$\text{with} \quad m_{jt}^{(i)} = \frac{1}{2}\left(\hat{e}_{jt}^{(i)_1} + \hat{e}_{jt}^{(i)_2}\right), \quad l_{jt}^{(i)} = \frac{\sqrt{3}}{2}\left(\hat{e}_{jt}^{(i)_2} - \hat{e}_{jt}^{(i)_1}\right) \quad (29)$$

with $j = r, s$ for i = D, E, F,

where $\hat{e}_{rt}^{(N)_k}$ and $\hat{e}_{st}^{(N)_k}$, with N = D, E, F, are calculated from Eq. (21). The tying positions $(D)_k$, $(E)_k$, $(F)_k$, with k = 1, 2, are shown in Fig. 2(b).

The assumed covariant transverse shear strain fields for the proposed shell elements are obtained by

$$e_{jt}^{AS} = \bar{e}_{jt}^{AS} + \hat{e}_{jt}^{AS} \quad \text{with } j = r, s. \quad (30)$$

Then, the element stiffness is constructed in the same manner as for the standard displacement-based shell element using the appropriate stress-strain matrix for shells. Since the order of the displacement interpolations is quadratic, the stiffness matrix is evaluated by the seven-point Gauss integration.

3. Convergence studies

In this section, convergence studies for the new shell elements (S3PU8 and S3PU4), as well as the enriched MITC3 with the updated formulation, are performed on the well-established plate and shell problems: a fully clamped plate problem, cylindrical shell problems, and hyperboloid shell problems. Since the finite element solutions are sensitive to element mesh patterns and distortions, two triangulated mesh patterns with uniform and distorted meshes as shown in Fig. 3 are considered in the tests below.

The s-norm (Hiller and Bathe 2003) is used to measure the convergence of the finite element solutions and is defined as follows:

$$\|\mathbf{u}_{\text{ref}} - \mathbf{u}_h\|_s^2 = \int_{\Omega_{\text{ref}}} \Delta\boldsymbol{\varepsilon}^T \Delta\boldsymbol{\tau}\, d\Omega_{\text{ref}} \quad (31)$$

$$\text{with} \quad \Delta\boldsymbol{\varepsilon} = \boldsymbol{\varepsilon}_{\text{ref}} - \boldsymbol{\varepsilon}_h \quad \text{and} \quad \Delta\boldsymbol{\tau} = \boldsymbol{\tau}_{\text{ref}} - \boldsymbol{\tau}_h$$

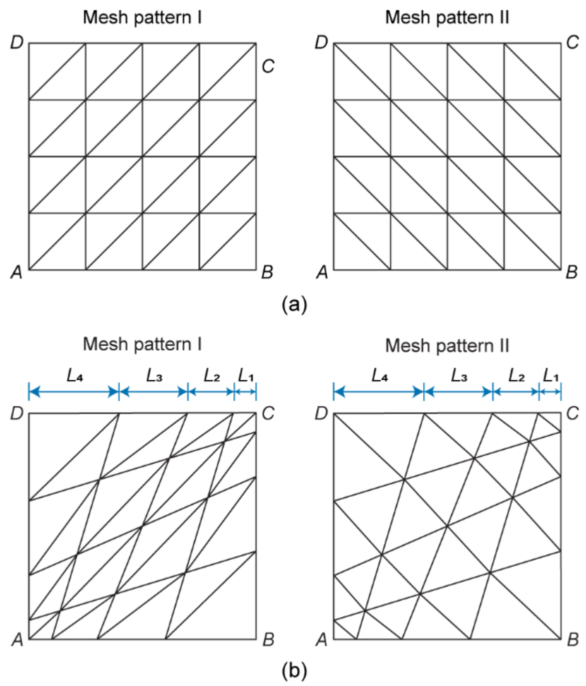

Fig. 3 Mesh Patterns I and II (a) and the corresponding distorted (b) meshes used (N = 4). For the $N \times N$ distorted mesh, each edge of the domain is divided by the ratio $L_1 : L_2 : L_3 : \ldots\ldots L_N$ = 1:2:3:…:N

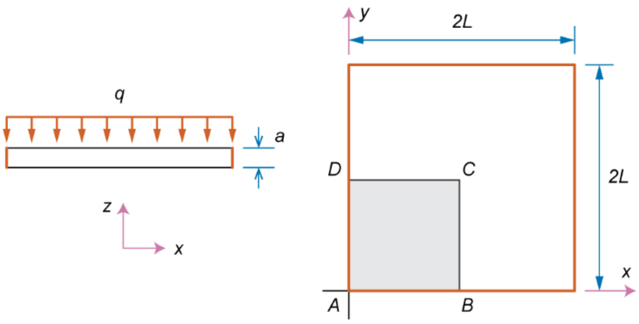

Fig. 4 Fully clamped square plate under uniform pressure ($L = 1$, $E = 1.7472 \times 10^7$, $q = 1$, and $\nu = 0.3$)

in which $\mathbf{u}_{\text{ref}}$ is a reference finite element solution, $\mathbf{u}_h$ is the solution obtained using the finite element discretization, and $\boldsymbol{\varepsilon}$ and $\boldsymbol{\tau}$ are the strain and stress vectors, respectively. The practical convergence can be estimated to be

$$\|\mathbf{u} - \mathbf{u}_h\|_s^2 \cong ch^k, \tag{32}$$

in which c is a constant and h denotes the element size. For the uniformly optimal shell element, the constant c is independent of the shell thickness, and k represents the optimal order of convergence, with $k = 2$ for the linear finite element and $k = 4$ for the second-order finite element.

The relative error for measuring the convergence of the finite elements in the problems below is given by

$$E_h = \frac{\|\mathbf{u}_{\text{ref}} - \mathbf{u}_h\|_s^2}{\|\mathbf{u}_{\text{ref}}\|_s^2}. \tag{33}$$

In the use of Eq. (33), the reference solutions are calculated with fine meshes of the MITC9 shell finite element, which produces accurate and reliable solutions (Bathe *et al.* 2003).

3.1 Fully clamped square plate problem

The plate shown in Fig. 4 is subjected to a uniform pressure load (Lee and Bathe 2004, Jeon *et al.* 2014, Lee *et al.* 2014). Because the plate is symmetric, only one-quarter of the plate (the shaded regions) is considered, using the appropriate symmetric boundary conditions $\bar{u}_x = \bar{\theta}_y = 0$ along BC, $\bar{u}_y = \bar{\theta}_x = 0$ along DC, and $\bar{u}_x = \bar{u}_y = \bar{u}_z = \bar{\theta}_x = \bar{\theta}_y = 0$ along AB and AD. Two mesh patterns (I and II) and the corresponding distorted meshes shown in Fig. 3 are considered.

The numerical reference solution is calculated with a 96 × 96 element mesh of MITC9 shell finite elements. The solutions are obtained with $N \times N$ element meshes; $N = 4$, 8, 16, 32, and 64 for the MITC3, enriched MITC3, S3PU8,

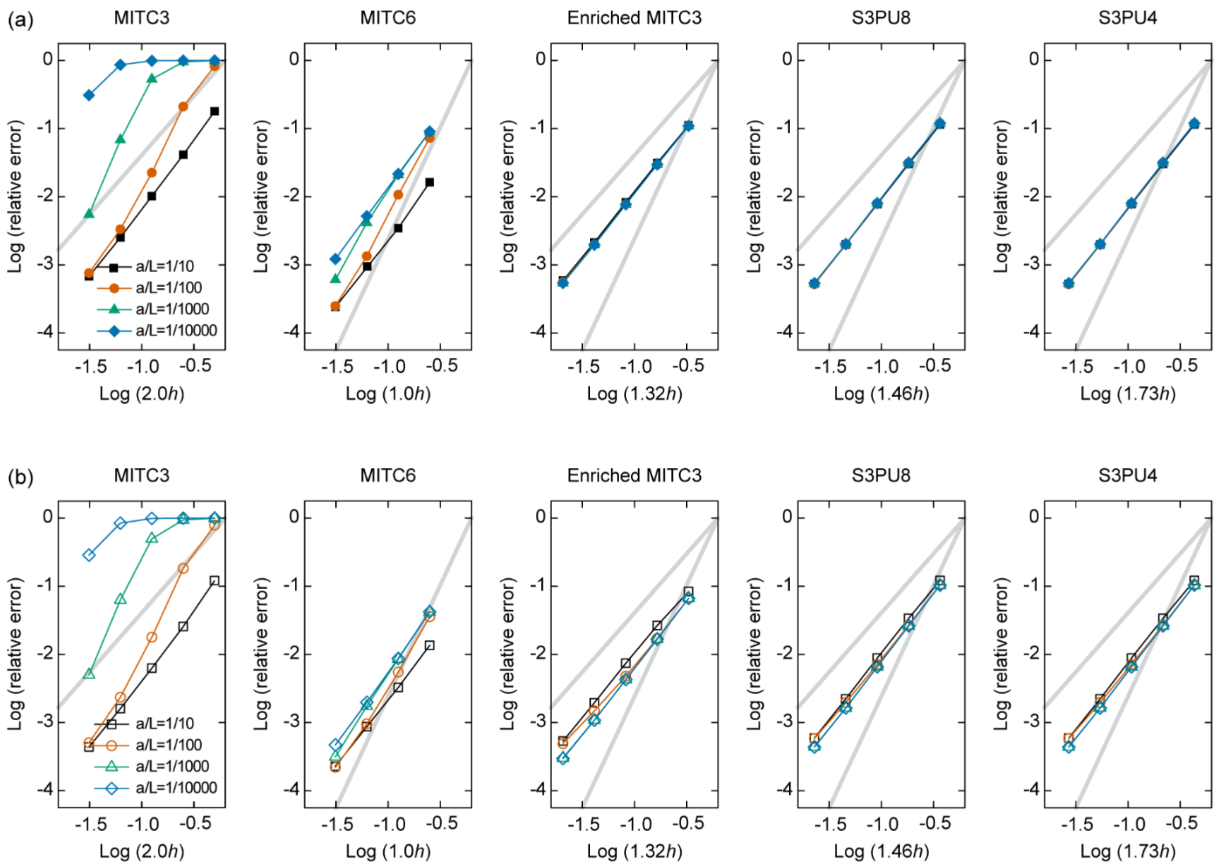

Fig. 5 Convergence curves for the fully clamped square plate problem when uniform meshes (Fig. 3) with Mesh Patterns I (a) and II (b) are used. The bold gray line in each graph represents the optimal convergence rate, which is 2.0 for linear elements and 4.0 for quadratic elements

and S3PU4 shell elements, and $N = 4$, 8, 16, and 32 for the MITC6 shell element. All convergence studies are tested with four different plate thicknesses (a/L = 1/10, 1/100, 1/1,000, and 1/10,000), and the "element size" used is $h = L/N$. To compare the convergence behaviors for the different shell elements, we use the equivalent element sizes 2.0h, 1.0h, 1.32h, 1.46h, and 1.73h for the MITC3, MITC6, enriched MITC3, and present (S3PU8, and S3PU4) shell elements, respectively.

Fig. 5 and Fig. 6 show the convergence curves for the fully clamped square plate problems using uniform and distorted meshes with two triangulated mesh patterns. The MITC3 shell element locks, and good accuracy characteristics are seen for a/L up to about 1/100. The solutions for the MITC3 and MITC6 shell elements are highly sensitive to the element mesh pattern and distortion. The convergence performances of the present (S3PU8 and S3PU4) and enriched MITC3 shell elements are almost optimal, even when distorted meshes are used (Fig. 6).

3.2 Cylindrical shell problems

The second example is a cylindrical shell with uniform thickness a, length 2L, and radius R, as shown in Fig. 7(a) (Lee and Bathe 2004, Jeon *et al.* 2014, Lee *et al.* 2014). The shell is subjected to a smoothly varying periodic pressure $p(\theta)$ normal to the shell surface:

$$p(\theta) = p_0 \cos(2\theta) \quad \text{with} \quad p_0 = 1. \tag{34}$$

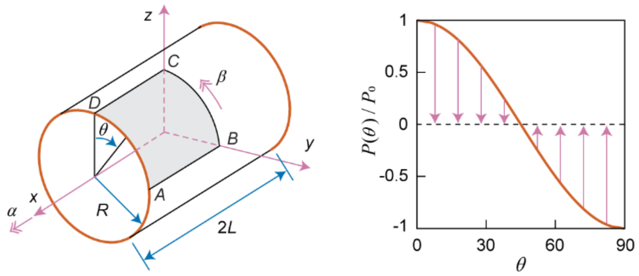

Fig. 7 Cylindrical shell problem ($L = R = 1$, $E = 2 \times 10^5$, and $\nu = 1/3$)

By applying different boundary conditions at both ends, we obtain two different asymptotic behaviors of the shell: the bending-dominated behavior under free boundary conditions and the membrane-dominated behavior under clamped boundary conditions. Utilizing the symmetry of the problem, we model only the shaded region *ABCD* in Fig. 7 with appropriate symmetric boundary conditions. For the membrane-dominated case, the clamped boundary condition is imposed: $\bar{u}_x = \bar{\beta} = 0$ along BC, $\bar{u}_y = \bar{\alpha} = 0$ along DC, $\bar{u}_z = \bar{\alpha} = 0$ along AB, and $\bar{u}_x = \bar{u}_y = \bar{u}_z = \bar{\alpha} = \bar{\beta} = 0$ along AD. For the bending-dominated case, the free boundary condition is imposed: $\bar{u}_x = \bar{\beta} = 0$ along BC, $\bar{u}_y = \bar{\alpha} = 0$ along DC, and $\bar{u}_z = \bar{\alpha} = 0$ along AB.

The numerical reference solution is calculated using a 96 × 96 element mesh of MITC9 shell finite elements for

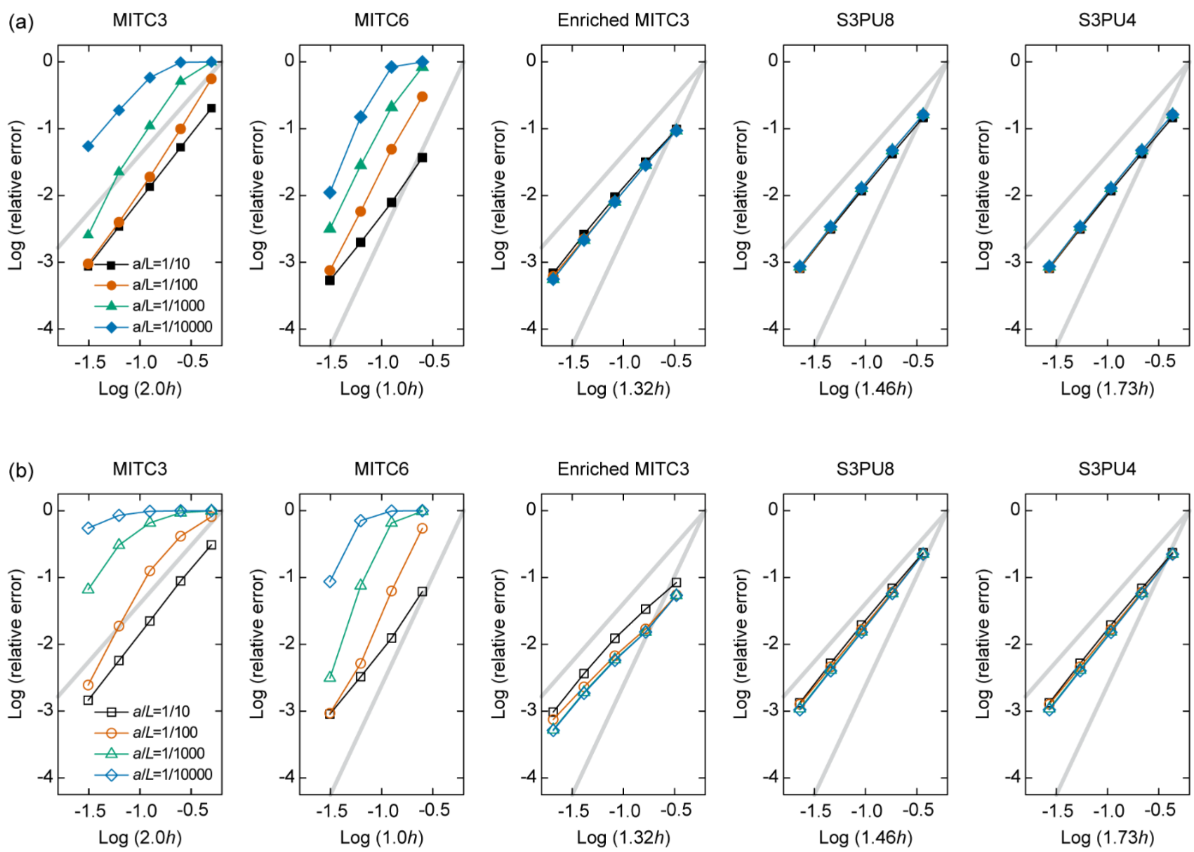

Fig. 6 Convergence curves for the fully clamped square plate problem when distorted meshes (Fig. 3) with Mesh Patterns I (a) and II (b) are used. The bold gray line in each graph represents the optimal convergence rate, which is 2.0 for linear elements and 4.0 for quadratic elements

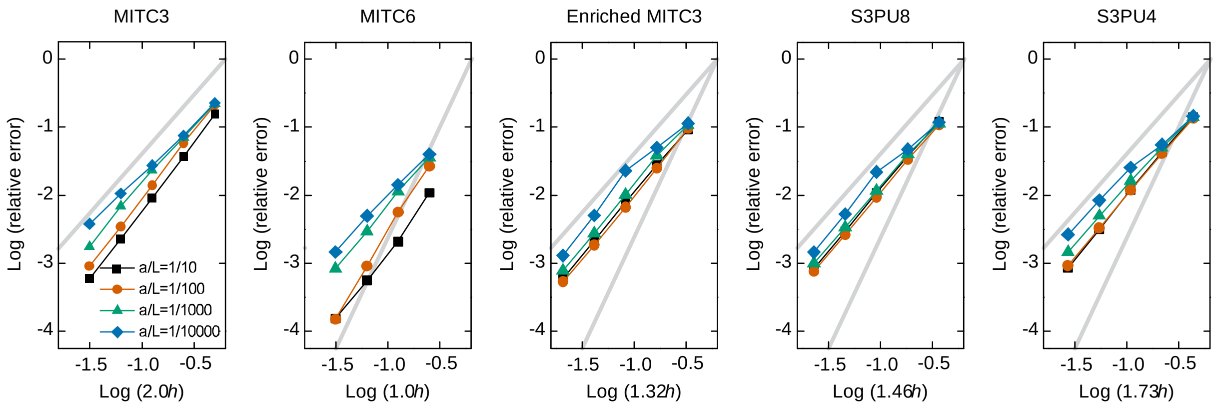

Fig. 8 Convergence curves for the clamped cylindrical shell problem with uniform Mesh Pattern I (Fig. 3). The bold gray line in each graph represents the optimal convergence rate, which is 2.0 for linear elements and 4.0 for quadratic elements

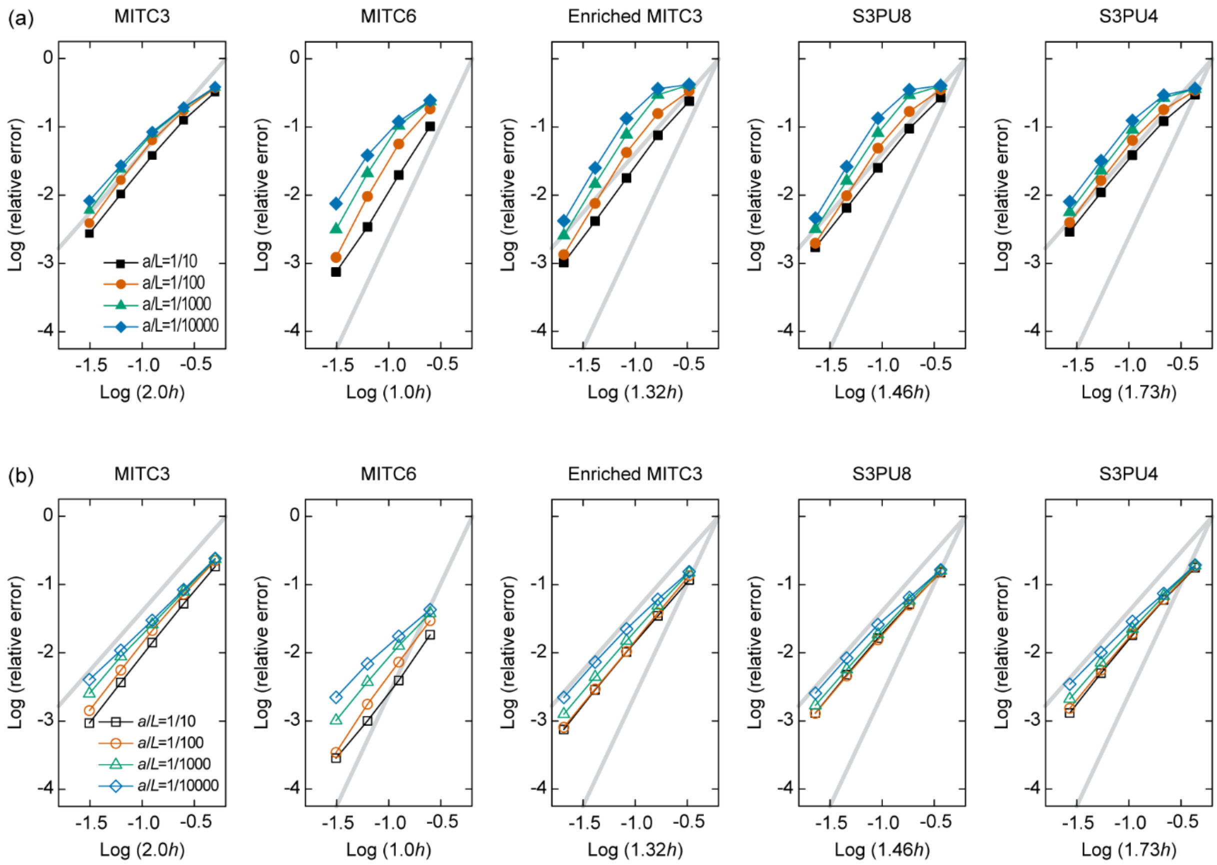

Fig. 9 Convergence curves for the clamped cylindrical shell problem when distorted meshes (Fig. 3) with Mesh Patterns I (a) and II (b) are used. The bold gray line in each graph represents the optimal convergence rate, which is 2.0 for linear elements and 4.0 for quadratic elements

both the membrane-dominated and the bending-dominated case. The solutions for the MITC3, MITC6, enriched MITC3, and present (S3PU8 and S3PU4) shell elements are obtained with $N \times N$ meshes (N = 4, 8, 16, 32, and 64 for the MITC3, enriched MITC3, S3PU8 and S3PU4 shell elements, and N = 4, 8, 16, and 32 for the MITC6 shell element). The distorted meshes with the two triangulated mesh patterns shown in Fig. 3 are also used in both cases.

The convergence curves for the clamped cylindrical shell problems with uniform and distorted meshes are shown in Fig. 8 and Fig. 9, respectively. The performances for the shell elements considered here show nearly optimal convergence behaviors regardless of the thickness of the shell.

Fig. 10 and Fig. 11 present the convergence curves for the free cylindrical shell problems with uniform and distorted meshes, respectively. When distorted meshes are used, the solutions of the MITC3 and MITC6 shell elements deteriorate as the shell thickness decreases, as a result of some locking. However, the PU-based shell elements exhibit good convergence behavior even when the distorted meshes are used.

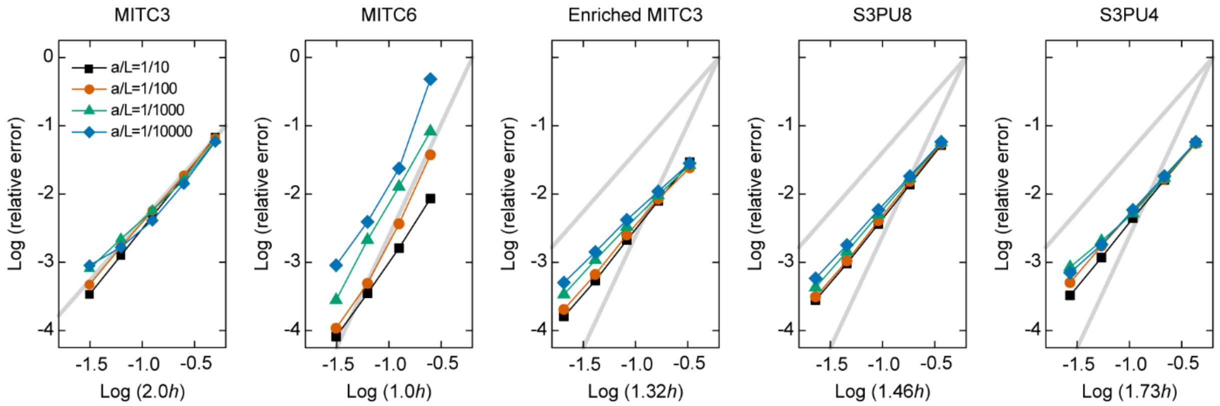

Fig. 10 Convergence curves for the free cylindrical shell problem with uniform Mesh Pattern I (Fig. 3). The bold gray line in each graph represents the optimal convergence rate, which is 2.0 for linear elements and 4.0 for quadratic elements

With the uniform mesh, the solutions for the clamped and free cylinder shell problems do not depend on element mesh patterns; thus, the convergence curves are considered only when Mesh Pattern I is used.

3.3 Hyperboloid shell problems

The third example is the hyperboloid shell shown in fig. 12(a) (Lee and Bathe 2004, Jeon *et al.* 2014, Lee *et al.* 2014). The mid-surface of the shell structure is modeled by

$$x^2 + y^2 = 1 + y^2; \qquad y \in [-1, \quad 1]. \tag{34}$$

A smoothly varying periodic pressure (Eq. (34) is applied normal to the surface, as in Fig. 7. When both ends are clamped, a membrane-dominated problem is obtained, and when the ends are free, a bending-dominated problem is obtained. It is well known that the bending-dominated hyperboloid shell problem is difficult to solve (Lee and Bathe 2004, Jeon *et al.* 2014) when the thickness is small. Because the shell element is symmetric, the analyses are carried out using one-eighth of the structure, corresponding to the shaded region *ABCD* in Fig. 12(a). For the membrane-dominated case, the boundary condition is imposed: $\bar{u}_z = \bar{\beta} = 0$ along *BC*, $\bar{u}_x = \bar{\beta} = 0$ along *AD*,

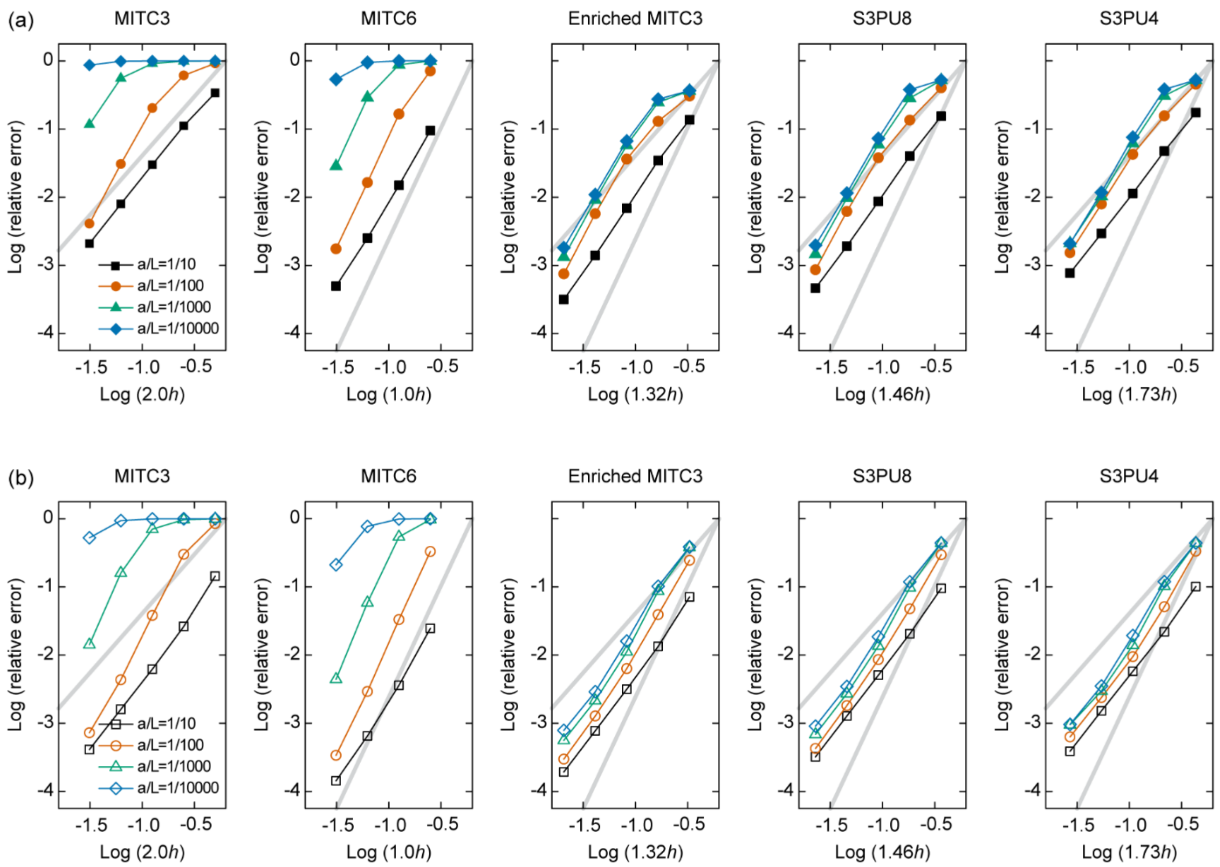

Fig. 11 Convergence curves for the free cylindrical shell problem when distorted meshes (Fig. 3) with Mesh Patterns I (a) and II (b) are used. The bold gray line in each graph represents the optimal convergence rate, which is 2.0 for linear elements and 4.0 for quadratic elements

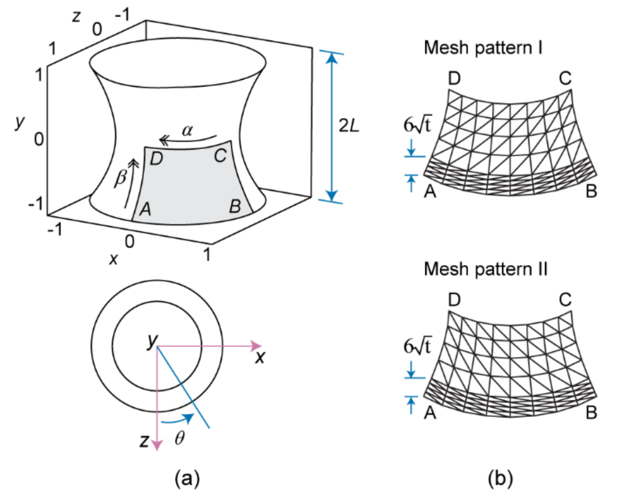

Fig. 12 Hyperboloid shell problem: (a) Problem description (E = 2 × 10^{11}, ν = 1/3). (b) Graded mesh for the clamped

$\bar{u}_y = \bar{\alpha} = 0$ along DC, and $\bar{u}_x = \bar{u}_y = \bar{u}_z = \bar{\alpha} = \bar{\beta} = 0$ along AB. For the bending-dominated case, the free boundary condition is imposed: $\bar{u}_z = \bar{\beta} = 0$ along BC, $\bar{u}_x = \bar{\beta} = 0$ along AD, and $\bar{u}_y = \bar{\alpha} = 0$ along DC.

The reference solutions are also calculated with a 96 × 96 mesh of MITC9 shell elements, and the solutions for the MITC3, MITC6, enriched MITC3, and present (S3PU8 and S3PU4) shell elements are obtained with $N \times N$ meshes (N = 4, 8, 16, 32, and 64 for the MITC3, enriched MITC3, S3PU8, and S3PU4 shell elements, and N = 4, 8, 16, and 32 for the MITC6 shell element). Only for the clamped hyperboloid shell problem do we use a boundary layer of width $6\sqrt{t}$ for half of the mesh (see Fig. 12 (b)).

The convergence curves for both uniform and distorted meshes in the membrane-dominated case are shown in Fig. 13 and Fig. 14, in which the solution accuracy is independent of the mesh patterns and all the shell elements show good performance when both uniform and distorted meshes are used.

The convergence curves for the bending-dominated case are shown in Fig. 15 and Fig. 16. The convergences for the MITC3 and MITC6 elements severely deteriorate when the thickness of the shell is small. The PU-based shell finite elements, such as the S3PU8, S3PU4, and enriched MITC3, show almost optimal convergence even when distorted meshes are used.

With the uniform mesh, the solutions for the clamped and free hyperboloid shell problems do not depend on element mesh patterns; thus, the convergence curves are considered only when Mesh Pattern I is used.

4. Convergence studies

In this section, the important aspect of the computational cost of the present elements (S3PU8 and S3PU4) is evaluated, comparing these elements' computational cost to that of the MITC6 and enriched MITC3 shell elements. First, the size and sparseness for the stiffness matrices are analyzed for the clamped cylindrical shell (shown in Fig. 7) discretized by the 6×6 element mesh. The patterns of the global stiffness matrices without imposing boundary conditions are shown in Fig. 17 (a), with colored squares presenting the non-zero entries and the size of the matrices corresponding to the total number of DOFs. The number of non-zero entries and the half-bandwidth are indicated at the bottom of each stiffness matrix.

In Reference (Jeon *et al.* 2014), it was reported that the enriched MITC3 shell element gives fewer equations and a smaller bandwidth than the MITC6 shell element; thus, the factorization time for the enriched MITC3 element is much smaller than for the MITC6 element using direct Gauss elimination. However, the number of non-zeros in the global stiffness matrix for the enriched MITC3 element is significantly larger than that in the corresponding matrix for the MITC6 element, leading to a different computational efficiency when the direct sparse solver (Schenk and Gärtner 2004), which provides the best overall performance in the vast majority of models, is used.

The total number of non-zeros for the S3PU8 shell element is much smaller than that for the enriched MITC shell element, but it still larger than that for the MITC6 shell element. The S3PU4 shell element, with 11,925 non-zeros and a half-bandwidth of 45, is much more effective and about 53% smaller than the MITC6 shell element. It is

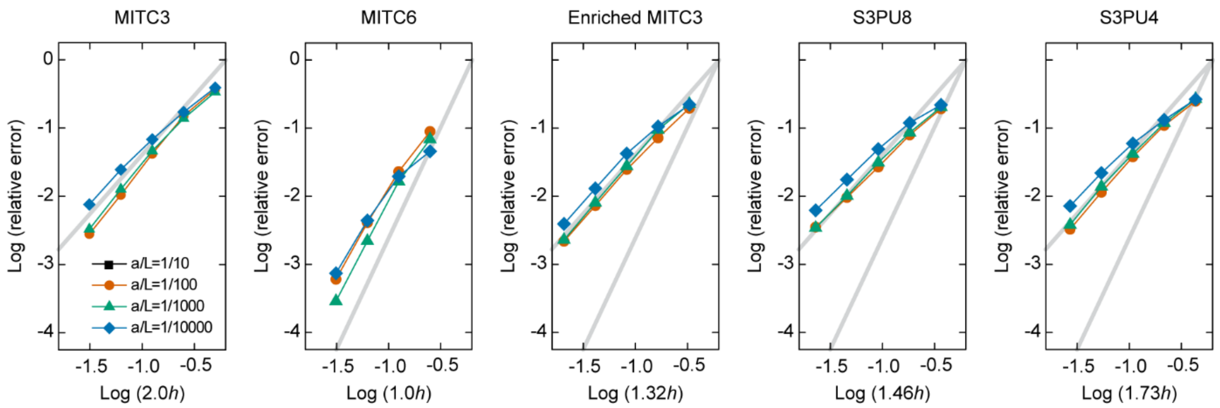

Fig. 13 Convergence curves for the clamped hyperboloid shell problem with uniform Mesh Pattern I (Fig. 3). The bold gray line in each graph represents the optimal convergence rate, which is 2.0 for linear elements and 4.0 for quadratic elements

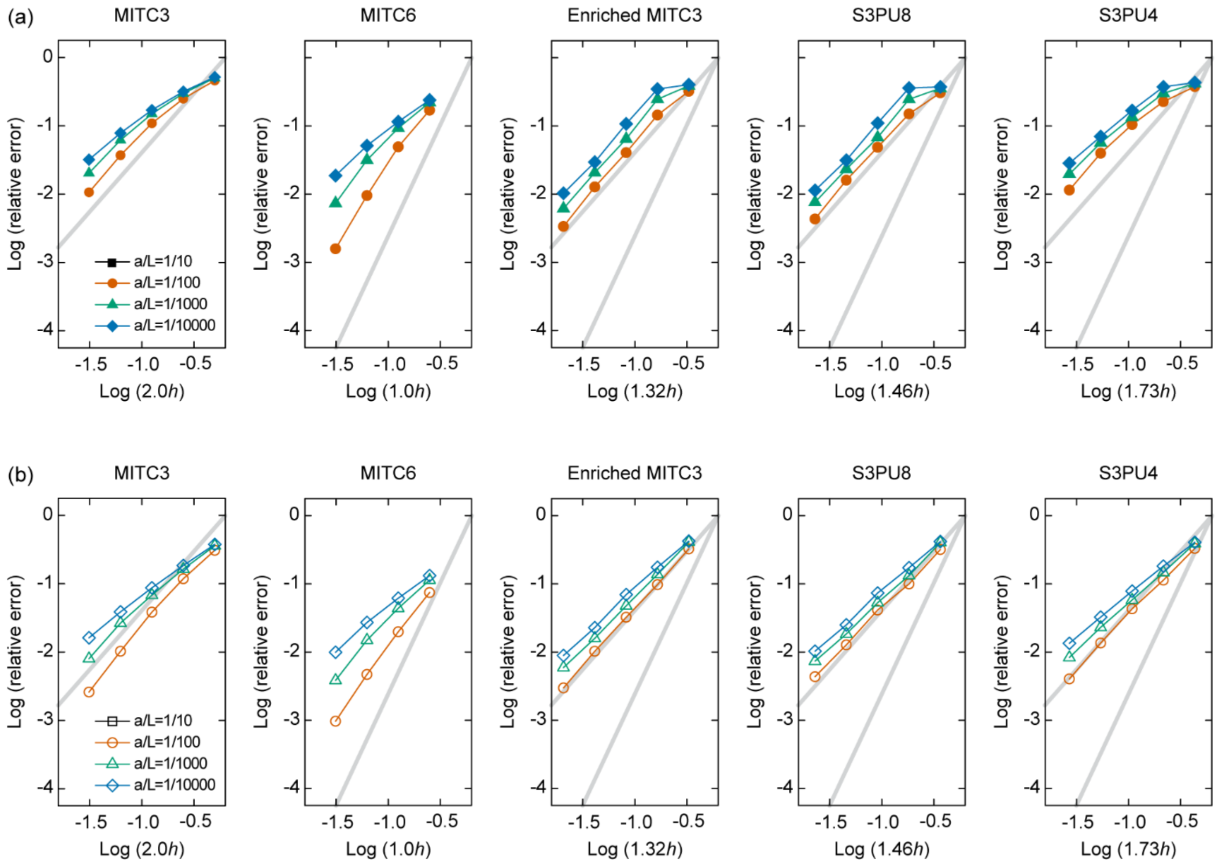

Fig. 14 Convergence curves for the clamped hyperboloid shell problem when distorted meshes (Fig. 3) with Mesh Patterns I (a) and II (b) are used. The bold gray line in each graph represents the optimal convergence rate, which is 2.0 for linear elements and 4.0 for quadratic elements

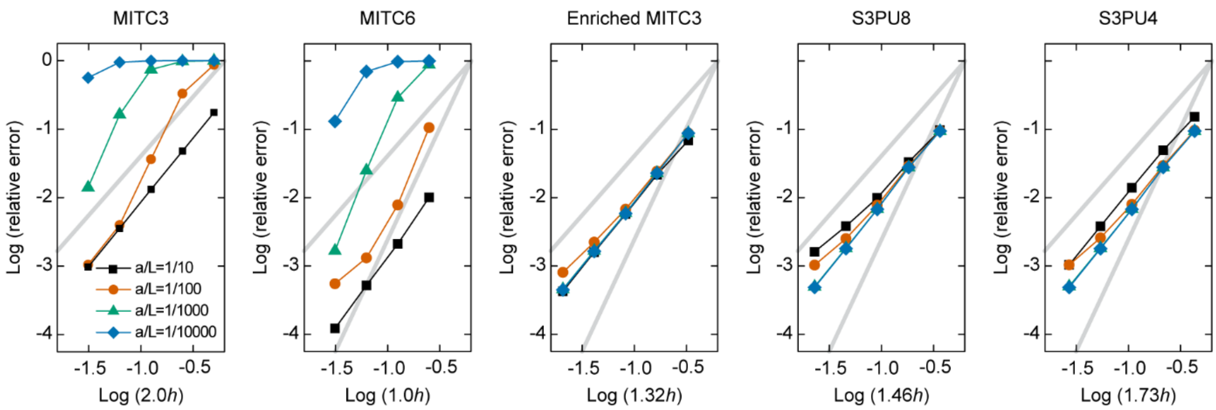

Fig. 15 Convergence curves for the free hyperboloid shell problem with uniform Mesh Pattern I (Fig. 3). The bold gray line in each graph represents the optimal convergence rate, which is 2.0 for linear elements and 4.0 for quadratic elements

valuable to compare the solution times required for the five shell finite elements considered here, using two different linear equation solvers: the skyline (Bathe 2014) and sparse (PARDISO, (Schenk and Gärtner 2004)) solvers. In all the cases, of course, symmetric stiffness matrices are generated.

The computational times for all the solution cases are tested on an Intel(R) Core i7 processor with 24 GB RAM on a Windows platform. As expected, the factorization time for the S3PU8 shell element is much smaller than that for the enriched MITC3 and MITC6 shell elements. Fig. 17(b) demonstrates the effectiveness of the S3PU8 shell element when the skyline solver is used. When the sparse solver is used, the solution time for the S3PU3 shell element is still higher than that for MITC6 shell element, but it has significantly decreased compared to the enriched MITC3 shell element (Fig. 17(c)).

5. Benchmark problems

In this section, three well-known benchmark problems are studied to test the efficacy of the proposed shell

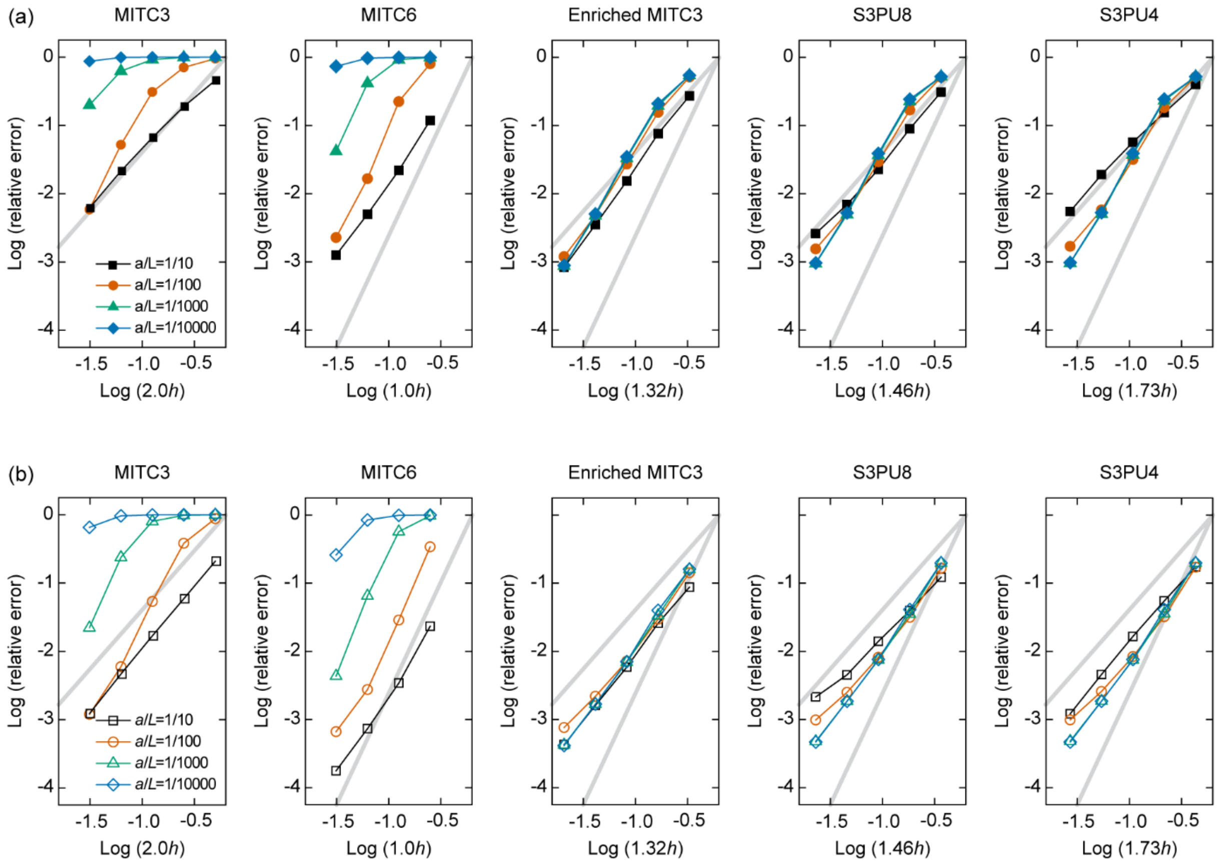

Fig. 16 Convergence curves for the free hyperboloid shell problem when distorted meshes (Fig. 3) with Mesh Patterns I (a) and II (b) are used. The bold gray line in each graph represents the optimal convergence rate, which is 2.0 for linear elements and 4.0 for quadratic elements

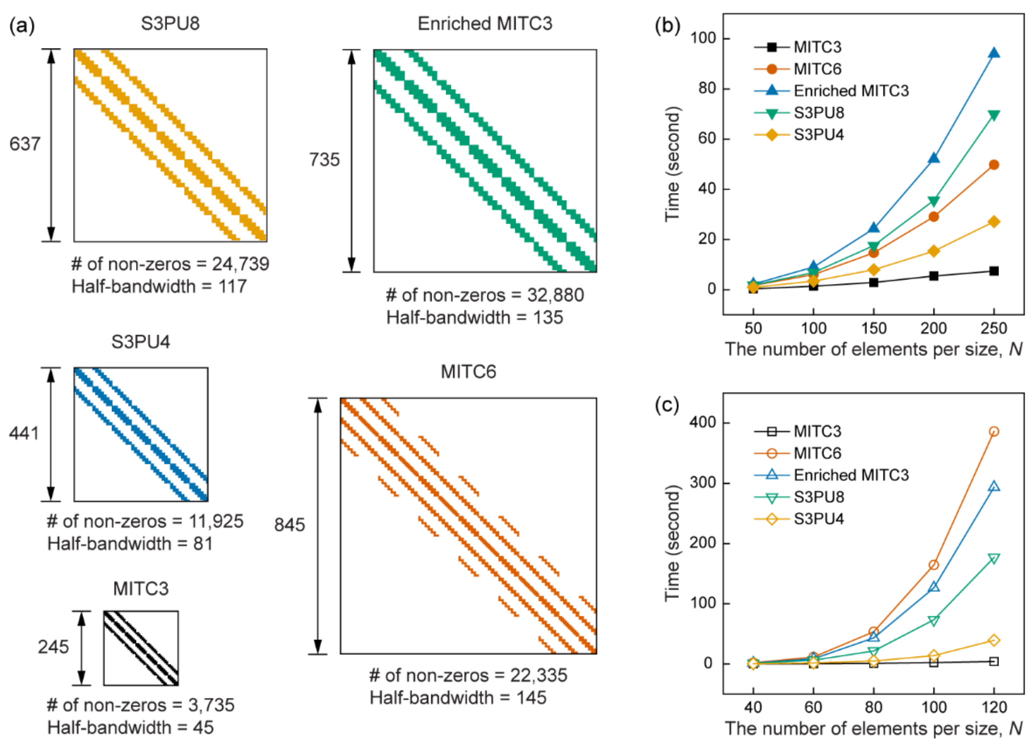

Fig. 17 Computational efficiency. (a) Stiffness matrix structures for MITC3, MITC6, enriched MITC3, S3PU8, and S3PU4 shell elements. The solution times for solving linear equations with skyline (b) and sparse (c) solvers

elements. The first two are bending-dominated shell problems, and the last is a membrane-dominated shell problem. Three triangulated mesh patterns (constant and mixed directional meshes) with uniform and distorted meshes are considered in the following benchmark tests.

5.1 Hyperbolic paraboloid shell problem

Fig. 18(a) shows a hyperbolic paraboloid shell of which the mid-surface is given by (Bathe *et al.* 2000)

$$z = y^2 - x^2\,; \qquad x, y \in [-1/2, \;\; 1/2]. \tag{36}$$

It is difficult to solve this problem owing to a doubly curved shell with negative Gaussian curvature. The shell is clamped at one edge and subjected to its own weight. Because of the symmetry problem, only one-half of the structure corresponding to the meshed region is considered.

The reference displacement at point A is established using a 144 × 72 mesh of MITC9 shell elements (w_{ref} = 2.878 × 10^{-4}). The solutions are calculated using $2N \times N$ element meshes with N = 4, 8, 12, 16, and 20. The uniform and distorted mesh patterns in Fig. 18(b) and (c) are used.

The convergence of the normalized displacement (w_A/w_{ref}) at point A is shown in Fig. 19. When the uniform mesh is used, the present (S3PU8 and S3PU4), enriched MITC3, and MITC6 shell elements show excellent performance, indicating that the PU-based shell elements are substantially better than the MITC6 shell element.

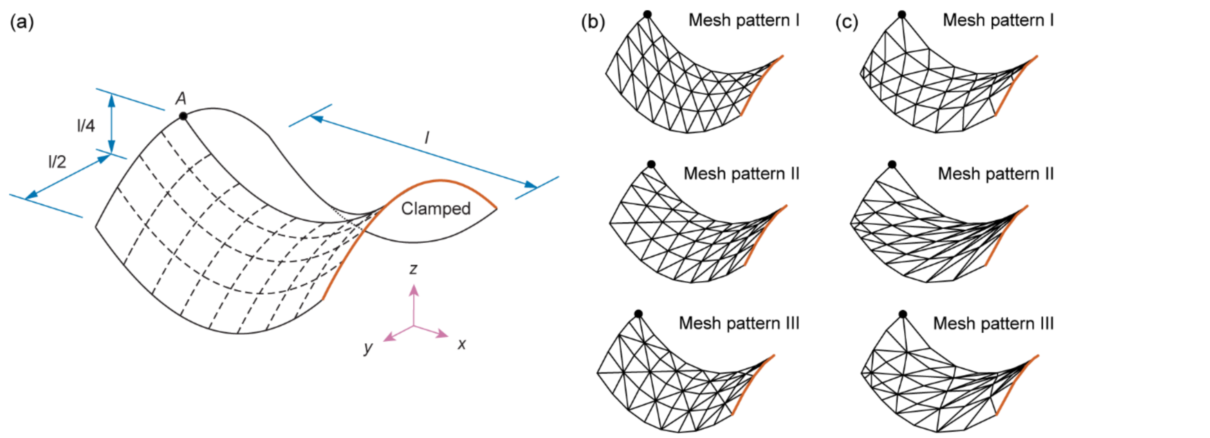

Fig. 18 Hyperbolic paraboloid shell problem. (a) Problem description (L = 1.0, thickness a = 0.001, density ρ = 360, acceleration of gravity $\mathbf{g}$ = 1.0, E = 2.0 × 10^{11}, and v = 0.3). Mesh Patterns I, II, and III (b) and the corresponding distorted mesh (c) patterns used (N=4)

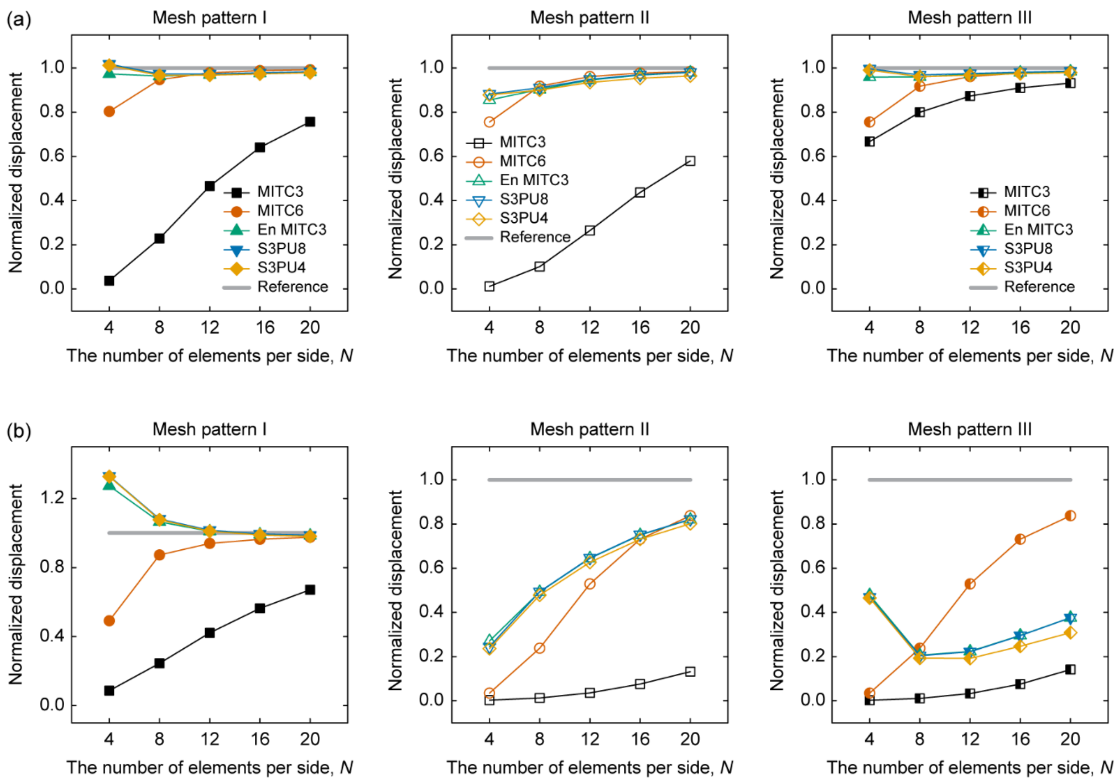

Fig. 19 Convergence of the normalized displacement at point A for the hyperbolic paraboloid shell with uniform (a) and distorted (b) meshes shown in Fig. 18

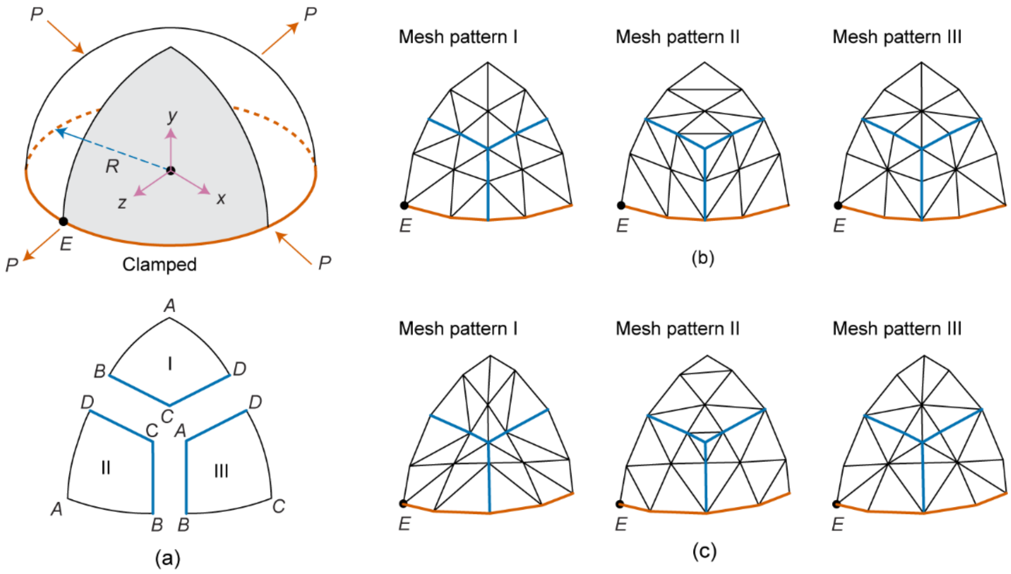

Fig. 20 Full-hemisphere shell problem. (a) Problem description (R =1 0, thickness a = 0.04, P = 2, E = 6.825 × 10^7 and ν = 0.3). Mesh Patterns I, II, and III (b) and the corresponding distorted mesh (c) patterns used (N = 2)

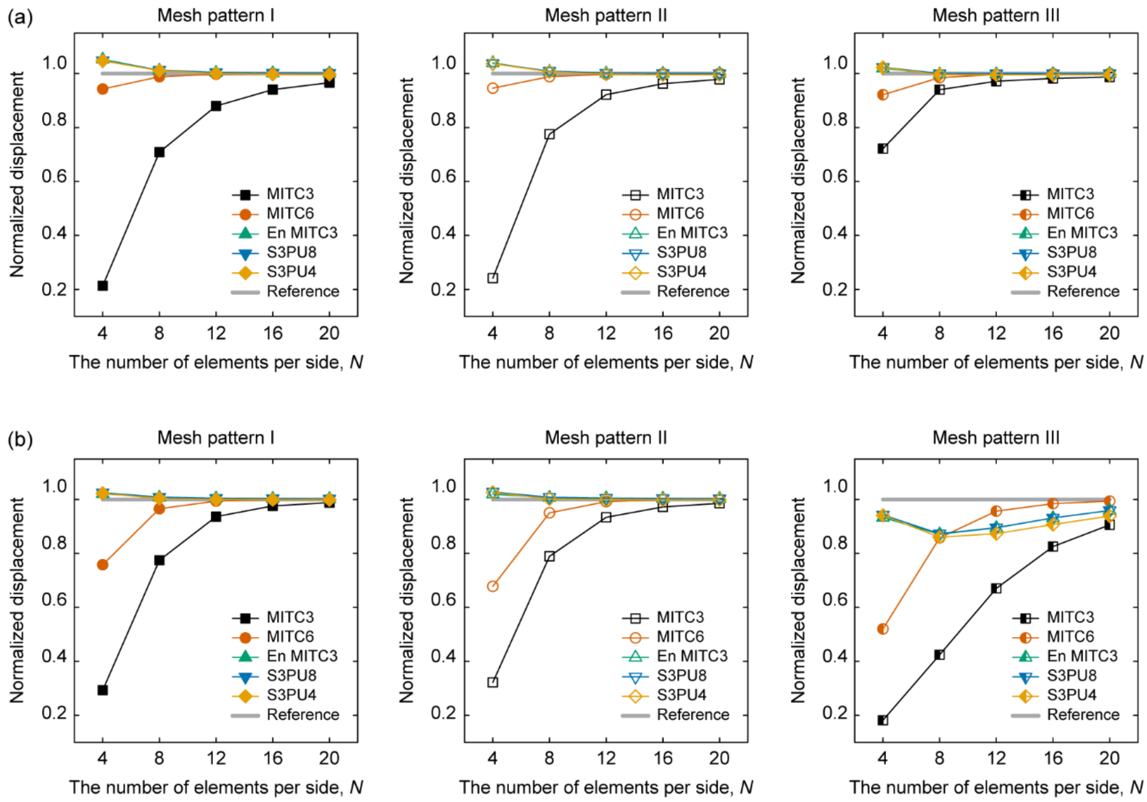

Fig. 21 Convergence of the normalized displacement at point E for the full-hemisphere shell with uniform (a) and distorted (b) meshes shown in Fig. 20

However, the PU-based shell elements show even worse convergence behavior than the MITC6 shell element when the Mesh Pattern III is distorted.

5.2 Full-hemisphere shell problem

The shell problem with a full hemisphere is shown in Fig. 20(a) (Jun *et al.* 2018a, Jun *et al.* 2018b). The hemisphere has radius R = 10, thickness a = 0.04, Young's modulus E = 6.825 × 10^7, and Poisson's ratio ν = 0.3. The hemisphere is subjected to two pairs of radial forces, P = 2. Using symmetry, we model one-quarter of the structure corresponding to the shaded region and consider three triangular mesh patterns (I, II, and III; Fig. 20(b)) as well as the corresponding distorted meshes (Fig. 20(c)).

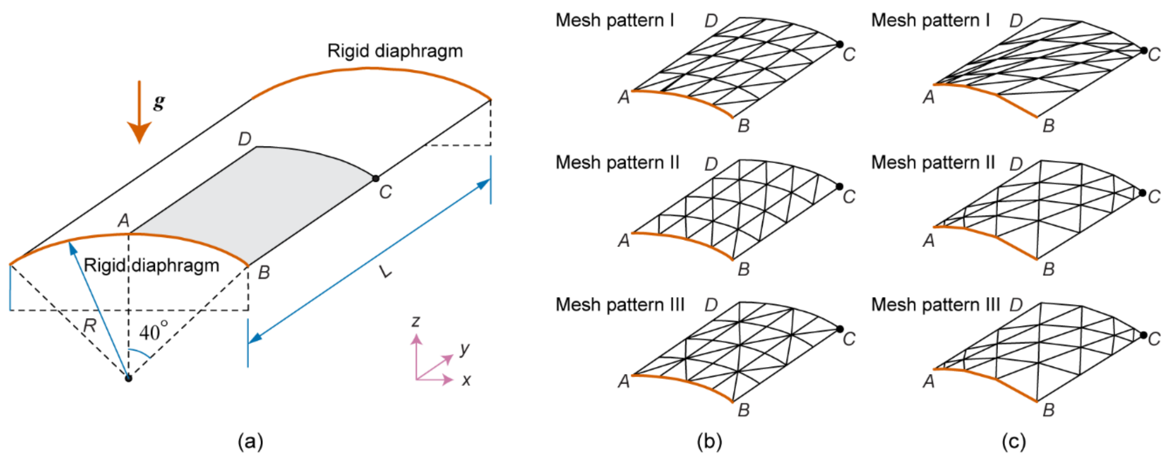

Fig. 22 Scordelis-Lo roof problem. (a) Problem description (L =5 0, R = 25, thickness a = 0.25, density ρ = 360, acceleration of gravity $\mathbf{g}$ = 1, $E = 4.32 \times 10^8$ and $\nu = 0$). Mesh Patterns I, II, and III (b) and the corresponding distorted mesh (c) patterns used (N = 4)

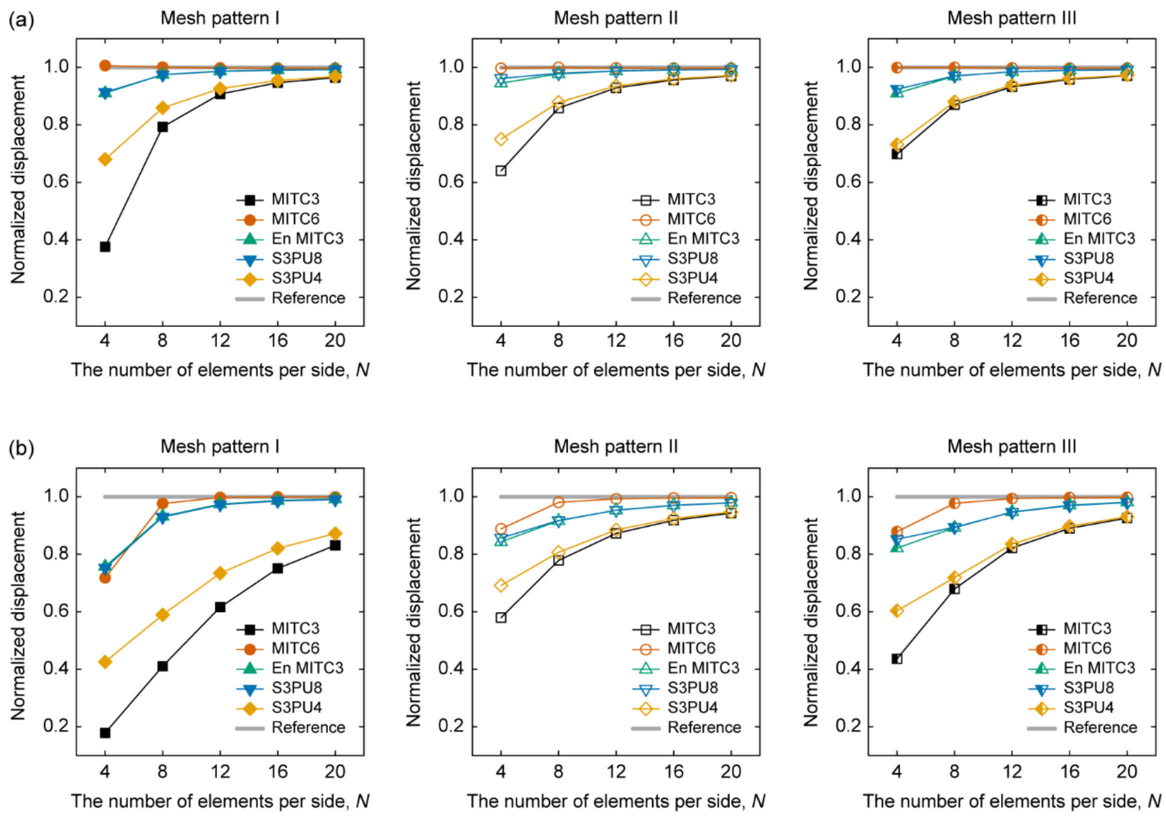

Fig. 23 Convergence of the normalized displacement at point C for the Scordelis-Lo roof with uniform (a) and distorted (b) meshes shown in Fig. 22

The solutions are obtained using the quadrant shell (shaded region) divided into three regions, 3 × (N × N) element meshes (N = 4, 8, 12, 16, and 20). The uniform and distorted mesh patterns in Fig. 20(b) and (c) are considered. The results are normalized by the reference solution of w_{ref} = 0.0924, given in Reference (Belytschko and Leviathan 1994).

The convergence of the normalized displacement (w_E/w_{ref}) at point E is presented in Fig. 21(a) for uniform meshes and in Fig. 21(b) for distorted meshes. The shell elements with the PU approximation converge well, whereas the performance of the other shell elements severely deteriorates when the distorted mesh is used.

5.3 Scordelis-Lo roof

The Scordelis-Lo roof is shown in Fig. 22(a). It is a classical benchmark problem for assessing the performance of shell elements (Jun *et al.* 2018a, Jun *et al.* 2018b). An asymptotically mixed bending-membrane behavior is observed. The roof structure is supported by rigid diaphragms at both ends. The radius of the curvature is R =

25, and the length and thickness of the roof are $L = 50$ and $t = 0.25$, respectively. The material has Young's modulus $E = 4.32 \times 10^8$ and Poisson's ratio $v = 0$. The roof is subjected to its own weight. Because of symmetry, only one-quarter of the shell corresponding to the shaded region *ABCD* in Fig. 22(a) is modelled, and the three mesh patterns (I, II, and III; Fig. 22(b)) and their corresponding distorted meshes (Fig. 22(c)) are considered.

The widely adopted reference solution for the vertical deflection at the center of the free edge (point *C*) is $w_{\text{ref}} = -0.3024$ (Belytschko and Leviathan 1994). The solutions are obtained using $N \times N$ element meshes ($N = 4$, 8, 12, 16, and 20). The convergence of the normalized displacement (w_C/w_{ref}) at point *C* is presented in Fig. 23(a) for uniform meshes and in Fig. 23(b) for distorted meshes. The MITC6, enriched MITC3, and S3PU8 shell elements exhibit better results, even though the distorted meshes are used.

It is well known that the solution and convergence behaviors of the triangular shell elements depend on the element mesh patterns (To and Liu 1994), showing better results for the element mesh with the triangulated mixed direction. However, the solutions of the shell elements considered here are significantly deteriorated when the mesh is distorted.

6. Conclusions

In this paper, two new PU-based shell finite elements, named S3PU8 and S3PU4, were proposed to decrease the total number of DOFs per node in the existing PU-based shell finite element (enriched MITC3) (Jeon *et al.* 2014), thereby maintaining the optimal convergence behavior and solution accuracy. The S3PU8 shell element, with 13 DOFs per node, is formulated by applying the PU approximation to both membrane displacements and rotations of the shell, giving excellent performances similar to those of the enriched MITC3 shell element in both membrane- and bending-dominated shell problems. The S3PU4 shell finite element is modeled by constructing a PU approximation with only rotations of the shell. This shell element is more effective than other PU-based shell finite elements and shows excellent convergence behavior in bending-dominated shell problems. Here, it is reported that the formulation for the enriched MITC3 shell element is updated by projecting linear polynomials to the membrane surface of the shell. Numerical tests show optimal convergence characteristics and excellent performances for the proposed shell elements, as compared to other MITC shell elements. In summary, although much remains to be investigated, the potential of the new shell elements is very attractive. Future work might pursue developing a method for nonlinear analysis and solving domains involving multiple corners and cracks.

References

Babuška, I. and Melenk, J.M. (1997), "The partition of unity method", *Int. J. Numer. Methods Eng.*, **40**, 727-758. https://doi.org/10.1002/(SICI)1097-0207(19970228)40:4%3C727::AID-NME86%3E3.0.CO;2-N.

Bathe, K.J. (2016), *Finite Element Procedures*, 2nd Edition, Higher Education Press, China.

Bathe, K.J. and Dvorkin, E.N. (1986), "A formulation of general shell elements-the use of mixed interpolation of tensorial components", *Int. J. Numer. Methods Eng.*, **22**, 697-722. https://doi.org/10.1002/nme.1620220312.

Bathe, K.J., Iosilevich, A. and Chapelle, D. (2000), "An inf-sup test for shell finite elements", *Comput. Struct.*, **75**, 439-456. https://doi.org/10.1016/S0045-7949(99)00213-8.

Bathe, K.J., Lee, P.S. and Hiller, J.F. (2003), "Towards improving the MITC9 shell element", *Comput. Struct.*, **81**, 477-489. https://doi.org/10.1016/S0045-7949(02)00483-2.

Belytschko, T. and Leviathan, I. (1994), "Physical stabilization of the 4-node shell element with one point quadrature", *Comput. Methods Appl. Mech. Eng.*, **113**, 321-350. https://doi.org/10.1016/0045-7825(94)90052-3.

Belytschko, T., Gracie, R. and Ventura, G. (2009), "A review of extended/generalized finite element methods for material modeling", *Model. Simul. Mater. Sci. Eng.*, **17**. https://doi.org/10.1088/0965-0393/17/4/043001.

Cai, Y., Zhuang, X. and Augarde, C. (2010), "A new partition of unity finite element free from the linear dependence problem and possessing the delta property", *Comput. Methods Appl. Mech. Eng.*, **199**, 1036-1043. https://doi.org/10.1016/j.cma.2009.11.019.

Cook, R.D. (2007), *Concepts and Applications of Finite Element Analysis*, John Wiley & Sons, New Jersey, USA.

Duarte, C.A., Babuška, I. and Oden, J.T. (2000), "Generalized finite element methods for three-dimensional structural mechanics problems", *Comput. Struct.*, **77**, 215-232. https://doi.org/10.1016/S0045-7949(99)00211-4.

Duarte, C.A., Hamzeh, O.N., Liszka, T.J. and Tworzydlo, W.W. (2001), "A generalized finite element method for the simulation of three-dimensional dynamic crack propagation", *Comput. Methods Appl. Mech. Eng.*, **190**, 2227-2262. https://doi.org/10.1016/S0045-7825(00)00233-4.

Hiller, J.F. and Bathe, K.J. (2003), "Measuring convergence of mixed finite element discretizations: an application to shell structures", *Comput. Struct.*, **81**, 639-654. https://doi.org/10.1016/S0045-7949(03)00010-5.

Hughes, T.J.R. (2012), *The Finite Element Method: Linear Static and Dynamic Finite Element Analysis*, Courier Corporation, MA, USA.

Jeon, H.M., Lee, P.S. and Bathe, K.J. (2014), "The MITC3 shell finite element enriched by interpolation covers", *Comput. Struct.*, **134**, 128-142. https://doi.org/10.1016/j.compstruc.2013.12.003.

Jeon, H.M., Lee, Y., Lee, P.S. and Bathe, K.J. (2015), "The MITC3+ shell element in geometric nonlinear analysis", *Comput. Struct.*, **146**, 91-104. https://doi.org/10.1016/j.compstruc.2014.09.004.

Jun, H., Yoon, K., Lee, P.S. and Bathe, K.J. (2018), "The MITC3+ shell element enriched in membrane displacements by interpolation covers", *Comput. Methods Appl. Mech. Eng.*, **337**, 458-480. https://doi.org/10.1016/j.cma.2018.04.007.

Jun, H., Mukai, P. and Kim, S. (2018), "Benchmark tests of MITC triangular shell elements", *Struct. Eng. Mech.*, **68**, 17-38. https://doi.org/10.12989/sem.2018.68.1.017.

Katili, A.M., Maknun, I.J. and Katili, I. (2019), "Theoretical equivalence and numerical performance of T3ys and MITC3 plate finite elements", *Struct. Eng. Mech.*, **69**, 527-536. https://doi.org/10.12989/sem.2019.69.5.527.

Lee, P.S. and Bathe, K.J. (2004), "Development of MITC isotropic triangular shell finite elements", *Comput. Struct.*, **82**, 945-962. https://doi.org/10.1016/j.compstruc.2004.02.004.

Lee, P.S., Noh, H.C. and Choi, C.K. (2008), "Geometry-dependent MITC method for a 2-node iso-beam element", *Struct. Eng. Mech.*, **29**, 203-221. https://doi.org/10.12989/sem.2008.29.2.203.

Lee, Y., Lee, P.S. and Bathe, K.J. (2014), "The MITC3+ shell element and its performance", *Comput. Struct.*, **138**, 12-23. https://doi.org/10.1016/j.compstruc.2014.02.005.

Lee, Y., Jeon, H.M., Lee, P.S. and Bathe, K.J. (2015), "The modal behavior of the MITC3+ triangular shell element", *Comput. Struct.*, **153**, 148-164. https://doi.org/10.1016/j.compstruc.2015.02.033.

Melenk, J.M. and Babuška, I. (1996), "The partition of unity finite element method: Basic theory and applications", *Comput. Methods Appl. Mech. Eng.*, **139**, 289-314. https://doi.org/10.1016/S0045-7825(96)01087-0.

Moës, N. and Belytschko, T. (2002), "Extended finite element method for cohesive crack growth", *Eng. Fract. Mech.*, **69**, 813-833. https://doi.org/10.1016/S0013-7944(01)00128-X.

Oden, J.T., Duarte, C.A.M. and Zienkiewicz, O.C. (1998), "A new cloud-based hp finite element method", *Comput. Methods Appl. Mech. Eng.*, **153**, 117-126. https://doi.org/10.1016/S0045-7825(97)00039-X.

Rajendran, S. and Zhang, B.R. (2007), "A "FE-meshfree" QUAD4 element based on partition of unity", *Comput. Methods Appl. Mech. Eng.*, **197**, 128-147. https://doi.org/10.1016/j.cma.2007.07.010.

Schenk, O. and Gärtner, K. (2004), "Solving unsymmetric sparse systems of linear equations with PARDISO", *Future Gener. Comput. Syst.*, **20**, 475-487. https://doi.org/10.1016/j.future.2003.07.011.

Shi, G.H. (1991), "Manifold method of material analysis", Transactions of the 9th army conference on applied mathematics and computing, Report No. 92-1, US Army Research Office, USA.

Shojaee, S., Ghelichi, M. and Izadpanah, E. (2013), "Combination of isogeometric analysis and extended finite element in linear crack analysis", *Struct. Eng. Mech.*, **48**, 125-150. https://doi.org/10.12989/sem.2013.48.1.125.

Strouboulis, T., Babuška, I. and Copps, K. (2000), "The design and analysis of the Generalized Finite Element Method", *Comput. Methods Appl. Mech. Eng.*, **181**, 43–69. https://doi.org/10.1016/S0045-7825(99)00072-9.

Strouboulis, T., Copps, K. and Babuška, I. (2001), "The generalized finite element method", *Comput. Methods Appl. Mech. Eng.*, **190**, 4081-4193. https://doi.org/10.1016/S0045-7825(99)00072-9.

Tian, R., Yagawa, G. and Terasaka, H. (2006), "Linear dependence problems of partition of unity-based generalized FEMs", *Comput. Methods Appl. Mech. Eng.*, **195**, 4768-4782. https://doi.org/10.1016/j.cma.2005.06.030.

To, C.W.S. and Liu, M.L. (1994), "Hybrid strain based three-node flat triangular shell elements", *Finite Elem. Anal. Des.*, **17**, 169-203. https://doi.org/10.1016/0168-874X(94)90080-9.

Xu, J.P. and Rajendran, S. (2013), "A 'FE-Meshfree' TRIA3 element based on partition of unity for linear and geometry nonlinear analyses", *Comput. Mech.*, **51**, 843-864. https://doi.org/10.1007/s00466-012-0762-2.

Yang, Y., Chen, L., Tang, X., Zheng, H. and Liu, Q. (2017), "A partition-of-unity based 'FE-Meshfree' hexahedral element with continuous nodal stress", *Comput. Struct.*, **178**, 17-28. https://doi.org/10.1016/j.compstruc.2016.10.012.

Zhang, B.R. and Rajendran, S. (2008), "'FE-Meshfree' QUAD4 element for free-vibration analysis", *Comput. Methods Appl. Mech. Eng.*, **197**, 3595-3604. https://doi.org/10.1016/j.cma.2008.02.012.

Zheng, H. and Xu, D. (2014), "New strategies for some issues of numerical manifold method in simulation of crack propagation", *Int. J. Numer. Methods Eng.*, **97**, 986-1010. https://doi.org/10.1002/nme.4620.